Draft version November 12, 2025
Typeset using LaTeX **twocolumn** style in AASTeX7.0.1

Mass Density Profiles in Globular and Open Clusters: A Comparative Study of M2 and M34

Nathan Madsen [1] and Chiara Caserta Lopez [1, 2]
Physics 134L

[1] *University of California, Santa Barbara*
[2] *Universidad Complutense de Madrid*

ABSTRACT

Star clusters serve as fundamental laboratories for understanding stellar evolution and galactic dynamics. We present a comparative study of mass density profiles in two representative stellar systems: the globular cluster M2 and the open cluster M34. M2, located in Aquarius, is an ancient (∼13 Gyr) and massive globular cluster with over 150,000 stars, while M34 in Perseus is a younger (∼200 Myr) open cluster with several hundred members. This study develops a comprehensive observational methodology for deriving accurate density profiles, including signal-to-noise calculations for observation planning, completeness corrections using artificial star tests with maximum likelihood estimation, and rigorous membership determination combining color-magnitude diagram filtering, Gaia proper motion analysis, and spatial distribution modeling. We employ the Plummer model as a theoretical framework to characterize the density profiles of both clusters. The contrasting properties of these systems—age, mass, concentration, and dynamical state—make them ideal testbeds for understanding how stellar systems evolve and disperse over cosmic timescales. This work establishes the data reduction pipeline and statistical methodology necessary for future photometric analysis of these clusters.

Keywords: Globular star clusters (656) — Open star clusters (1160) — Stellar density (1622) — Stellar populations (1622) — Photometry (1234) — Astrometry (80)

1. INTRODUCTION

Star clusters are gravitationally bound systems of stars that formed from the same giant molecular cloud, providing natural laboratories for studying stellar evolution, dynamical processes, and galactic structure. These systems can be broadly classified into two main types: globular clusters and open clusters, which differ dramatically in age, mass, stellar population, and dynamical state.

1.1. *Star Clusters as Astrophysical Laboratories*

Globular clusters are among the oldest objects in the Galaxy, with ages typically exceeding 10 billion years. They contain hundreds of thousands to millions of stars in compact, spherically symmetric configurations with high central densities. Their ancient stellar populations, low metallicities, and tight gravitational binding make them valuable probes of the early Galaxy and stellar evolution at low metallicity. In contrast, open clusters are younger systems, ranging from a few million to a few billion years old, containing tens to thousands of stars in loosely bound configurations. These clusters are found primarily in the Galactic disk and provide insights into recent star formation and the evolution of solar-metallicity stars.

The mass density profile—the distribution of stellar mass as a function of radius from the cluster center—is a fundamental property that encodes information about a cluster's formation, dynamical evolution, and ultimate fate. Measuring accurate density profiles requires addressing several observational challenges: photometric completeness at faint magnitudes, contamination from field stars, and the characterization of observational uncertainties.

1.2. *The Plummer Model*

The Plummer model, proposed by H. C. Plummer (1911) as a mathematical description of globular clusters, provides a simple yet physically motivated framework for characterizing spherical stellar systems. The

Email: madsen@ucsb.edu

model is defined by its gravitational potential:

$$\Phi(r) = -\frac{GM}{\sqrt{r^2 + a^2}} \tag{1}$$

where G is the gravitational constant, M is the total cluster mass, and a is the Plummer radius, a scale parameter characterizing the size of the cluster core.

The corresponding mass density distribution can be derived from Poisson's equation, $\nabla^2\Phi = 4\pi G\rho$. For a spherically symmetric system, this yields:

$$\rho(r) = \frac{3M}{4\pi a^3}\left(1 + \frac{r^2}{a^2}\right)^{-5/2} \tag{2}$$

This profile exhibits two key features: (1) a constant-density core as $r \to 0$, with $\rho(0) = 3M/(4\pi a^3)$, and (2) a steep power-law decline $\rho(r) \propto r^{-5}$ at large radii. While more sophisticated models (e.g., King, Wilson, and Michie-King models) better describe observed clusters by incorporating effects such as tidal truncation and anisotropic velocity dispersions, the Plummer model's analytical tractability makes it an excellent starting point for characterizing cluster structure.

1.3. *Our Target Clusters: M2 and M34*

We focus on two clusters that exemplify the extremes of the cluster population: M2 (NGC 7089), a massive globular cluster, and M34 (NGC 1039), a nearby open cluster.

M2 is located in the constellation Aquarius at a distance of approximately 11.5 kpc. With an age of ∼12.5–13 Gyr and a metallicity of [Fe/H] ≈ -1.6, it represents the ancient, metal-poor stellar population characteristic of the Galactic halo. M2 contains over 150,000 stars within a half-light radius of ∼6 arcmin and exhibits the highly concentrated, spherically symmetric structure typical of dynamically evolved globular clusters. Its high central density and steep density gradient make it well-suited for testing the Plummer model and more complex dynamical models.

M34 is a young open cluster in Perseus, located at a distance of only ∼470 pc with an age of ∼200 Myr. It contains an estimated 100–400 members spread over a region ∼30 arcmin in diameter. Unlike M2, M34 has solar metallicity and a much lower stellar density, reflecting its recent formation and loose gravitational binding. The cluster's proximity to the Galactic plane results in significant field star contamination, making membership determination a critical component of the analysis. M34 is also more susceptible to tidal disruption from the Galactic potential, and its eventual dispersal is expected within a few hundred million years.

The stark contrasts between these systems—in age (13 Gyr vs. 200 Myr), mass ($\sim 10^5 M_\odot$ vs. $\sim 10^3 M_\odot$), density profile, and dynamical state—make them ideal comparative targets for understanding how stellar systems evolve and how observational techniques must be adapted to different astrophysical regimes.

2. METHODOLOGY

Deriving accurate stellar density profiles from photometric observations requires careful attention to observational planning, data reduction, and systematic error mitigation. This section outlines our comprehensive methodology, which includes signal-to-noise calculations for exposure time optimization, photometric completeness corrections via artificial star tests, and multi-dimensional membership determination to isolate cluster members from field star contamination.

2.1. *Signal-to-Noise Ratio and Observation Planning*

Accurate photometry requires sufficient signal-to-noise ratio (S/N) across the magnitude range of interest. We calculate the expected S/N for point sources using the CCD equation (S. B. Howell 2006):

$$\frac{S}{N} = \frac{FA_\epsilon\tau}{\sqrt{N_R^2 + \tau(FA_\epsilon + i_{DC} + F_\beta A_\epsilon\Omega)}} \tag{3}$$

where F is the target flux (photons s^{-1} m^{-2}), A_ϵ is the effective collecting area of the telescope (m^2), τ is the integration time (s), N_R is the readout noise (electrons), i_{DC} is the dark current (electrons s^{-1}), F_β is the sky background flux per solid angle (photons s^{-1} m^{-2} sr^{-1}), and Ω is the solid angle subtended by one pixel (sr).

The signal term, $S = FA_\epsilon\tau$, represents the total number of photons collected from the target star. The noise has four components: (1) readout noise N_R, a constant per exposure, (2) Poisson noise from the source itself $\sqrt{FA_\epsilon\tau}$, (3) dark current noise $\sqrt{i_{DC}\tau}$, and (4) sky background noise $\sqrt{F_\beta A_\epsilon\Omega\tau}$.

For multi-pixel aperture photometry, the effective noise scales with the number of pixels n_{pix} over which the source is distributed. The readout and background noise terms scale as $\sqrt{n_{pix}}$, while the source signal and source noise remain unchanged (assuming the aperture captures all source flux). This leads to a modified S/N:

$$\frac{S}{N} = \frac{FA_\epsilon\tau}{\sqrt{FA_\epsilon\tau + n_{pix}(N_R^2 + i_{DC}\tau + F_\beta A_\epsilon\Omega\tau)}} \tag{4}$$

Image Stacking: To improve S/N while avoiding saturation of bright stars, we employ image stacking. If N_{exp} independent exposures of duration τ are combined, the stacked S/N increases as:

$$(S/N)_{\text{stacked}} = \sqrt{N_{exp}} \times (S/N)_{\text{single}} \tag{5}$$

This technique is particularly valuable for observations of M34, where the dynamic range from the brightest members (V $\sim$ 11 mag) to the faintest detectable stars (V $\sim$ 19 mag) spans nearly 8 magnitudes.

Using Equation 3, we planned multi-band SDSS g' and r' observations with exposure times optimized to achieve S/N > 20 at the faint limit while maintaining S/N > 100 for bright cluster members through shorter individual exposures combined via stacking.

2.2. *Background Estimation and Subtraction*

Accurate aperture photometry requires precise characterization and removal of the sky background. The background in CCD images has multiple contributions: diffuse sky emission (zodiacal light, airglow, light pollution), unresolved faint stars, scattered light, and instrumental effects (E. Bertin & S. Arnouts 1996). Critically, the background is spatially varying due to gradients in sky brightness, flat-field residuals, and varying stellar density across the field.

We employ a 2D mesh-based background estimation algorithm. The image is divided into a grid of boxes (typically 64×64 pixels), and in each box we compute the sigma-clipped median to robustly estimate the local background level while rejecting outliers from bright sources. The sigma-clipping procedure iteratively removes pixels more than $\sigma_{\rm clip} = 3.0\sigma$ from the median (typically 5 iterations) to ensure that point sources do not bias the background estimate.

The box-level estimates are then median-filtered (filter size 3×3 boxes) to suppress residual noise and interpolated via bicubic splines to construct a smooth 2D background model $B(x, y)$ at full image resolution. This background-subtracted image, $I_{\rm sub}(x, y) = I_{\rm raw}(x, y) - B(x, y)$, is used for source detection and photometry.

The quality of background subtraction directly impacts photometric uncertainties. For aperture photometry, the total variance in a measurement includes contributions from the source Poisson noise, readout noise, and uncertainty in the background estimate:

$$\sigma^2_{\rm total} = \frac{F_\star}{g} + N_{\rm pix}\left(\frac{B}{g} + \left(\frac{\sigma_{\rm sky}}{g}\right)^2 + \left(\frac{R}{g}\right)^2\right) \qquad (6)$$

where $F_\star$ is the source counts, B is the background per pixel, $\sigma_{\rm sky}$ is the RMS background variation, R is the readout noise, g is the detector gain, and $N_{\rm pix}$ is the number of pixels in the aperture. Poor background estimation increases $\sigma_{\rm sky}$, degrading the S/N at faint magnitudes.

Appendix B provides a detailed description of the background estimation algorithm, validation tests on our M34 data, and diagnostic plots showing the 2D background model and residuals.

2.3. *Completeness Corrections*

Photometric surveys suffer from incompleteness at faint magnitudes due to detection limits, photometric uncertainties, and source crowding. The completeness function $C(m)$ is defined as the fraction of stars at true magnitude m that are successfully detected and measured:

$$C(m) \equiv \frac{N_{\rm detected}(m)}{N_{\rm true}(m)} \qquad (7)$$

The observed luminosity function $\Phi_{\rm obs}(m)$ is related to the intrinsic luminosity function by:

$$\Phi_{\rm obs}(m) = C(m) \cdot \Phi_{\rm true}(m) \qquad (8)$$

2.3.1. *Artificial Star Tests*

We determine $C(m)$ empirically using artificial star tests (P. B. Stetson 1990). For each magnitude bin m_i, we inject $N_{\rm add}$ artificial stars with known positions (x_j, y_j) and magnitudes into the science images, run the same photometric reduction pipeline, and measure the recovery fraction.

A star is considered "recovered" if a source is detected within a matching radius $r_{\rm match}$ (typically 1–2 pixels) and the recovered magnitude satisfies $|m_{\rm rec} - m_{\rm input}| < \Delta m_{\rm max}$:

$$\Delta r_{ij} = \sqrt{(x_i - x_j^{\rm rec})^2 + (y_i - y_j^{\rm rec})^2} < r_{\rm match} \qquad (9)$$

The completeness for magnitude bin m_i is:

$$C(m_i) = \frac{N_{\rm recovered}(m_i)}{N_{\rm added}(m_i)} \qquad (10)$$

2.3.2. *Maximum Likelihood Estimation*

Rather than using simple least-squares fitting, we employ maximum likelihood estimation (MLE) with proper binomial statistics. The number of recovered stars follows a binomial distribution:

$$P(N_{\rm rec}|N_{\rm add}, C) = \frac{N_{\rm add}!}{N_{\rm rec}!\,(N_{\rm add} - N_{\rm rec})!}\, C^{N_{\rm rec}}(1-C)^{N_{\rm add}-N_{\rm rec}} \qquad (11)$$

For a parametric completeness model $C(m; \theta)$, several functional forms have been proposed in the literature. The three most commonly used are:

Error Function (Gaussian CDF):

$$C_{\rm erf}(m; m_{50}, \sigma_{\rm comp}) = \frac{1}{2}\left[1 + {\rm erf}\left(\frac{m_{50} - m}{\sqrt{2}\sigma_{\rm comp}}\right)\right] \qquad (12)$$

Hyperbolic Tangent:

$$C_{\rm tanh}(m; m_{50}, \alpha) = \frac{1}{2}\left[1 + \tanh\left(\frac{m_{50} - m}{\alpha}\right)\right] \qquad (13)$$

Fermi-Dirac:

$$C_{\rm FD}(m; m_{50}, \Delta) = \frac{1}{1 + \exp\left(\frac{m - m_{50}}{\Delta}\right)} \tag{14}$$

In all three forms, m_{50} represents the magnitude at 50% completeness, while the second parameter ($\sigma_{\rm comp}$, α, or Δ) controls the transition width. These functional forms are mathematically very similar—differing primarily in their asymptotic tails—and produce nearly indistinguishable fits for typical photometric data. We adopt the error function form (Equation 12) as it naturally arises from assuming Gaussian photometric errors and has a direct physical interpretation: $\sigma_{\rm comp}$ represents the effective magnitude uncertainty at the detection threshold.

The log-likelihood across all magnitude bins is:

$$\ln \mathcal{L}(\theta) = \sum_{i=1}^{n} \left[N_{\rm rec,i} \ln C(m_i; \theta) + (N_{\rm add,i} - N_{\rm rec,i}) \ln(1 - C(m_i; \theta))\right] \tag{15}$$

We maximize Equation 15 to obtain the best-fit parameters $\hat{\theta}_{\rm MLE}$. Parameter uncertainties are estimated from the Fisher information matrix:

$$F_{jk} = -\left\langle \frac{\partial^2 \ln \mathcal{L}}{\partial \theta_j \partial \theta_k} \right\rangle, \quad {\rm Cov}(\theta) = F^{-1} \tag{16}$$

2.3.3. *Richardson-Lucy Deconvolution*

Simple division by $C(m)$ ignores photometric scatter, where stars at true magnitude m' may be observed at $m \neq m'$ due to measurement uncertainty. The observed distribution is a convolution:

$$\Phi_{\rm obs}(m) = \int K(m, m') \Phi_{\rm true}(m')\, dm' \tag{17}$$

where the kernel $K(m, m') = C(m') \cdot P(m|m')$ incorporates both completeness and photometric scatter, assumed to be Gaussian:

$$P(m|m') = \frac{1}{\sqrt{2\pi\sigma_m^2}} \exp\left[-\frac{(m - m')^2}{2\sigma_m^2}\right] \tag{18}$$

We apply the Richardson-Lucy algorithm (W. H. Richardson 1972; L. B. Lucy 1974), an iterative maximum-likelihood deconvolution method that enforces positivity. Starting from an initial guess $\Phi_{\rm true}^{(0)} = \Phi_{\rm obs}$, we iterate:

$$\Phi_{\rm true}^{(n+1)}(m') = \Phi_{\rm true}^{(n)}(m') \int \frac{\Phi_{\rm obs}(m)}{\int K(m, m'')\Phi_{\rm true}^{(n)}(m'')dm''} K(m, m')\, dm \tag{19}$$

until convergence (typically 20–50 iterations).

2.4. *Membership Determination*

Both M2 and M34 lie in regions with significant field star contamination. Accurate density profiles require isolating cluster members from foreground and background stars. We employ a Bayesian approach combining three independent membership criteria: color-magnitude diagram (CMD) filtering, proper motion analysis, and spatial distribution.

2.4.1. *Color-Magnitude Diagram Filtering*

Cluster members share common properties: age, metallicity, distance, and reddening. In the CMD, they follow a well-defined isochrone. We compute the perpendicular distance from each star to a theoretical isochrone, normalized by photometric uncertainties:

$$d_{\rm CMD}(i) = \min_j \sqrt{\left(\frac{g_i - g_{\rm iso,j}}{\sigma_g}\right)^2 + \left(\frac{(g-r)_i - (g-r)_{\rm iso,j}}{\sigma_{g-r}}\right)^2} \tag{20}$$

The CMD membership probability is modeled as:

$$P_{\rm CMD}(i) = \exp\left[-\frac{d_{\rm CMD}^2(i)}{2}\right] \tag{21}$$

2.4.2. *Proper Motion Filtering*

We use Gaia DR3 (Gaia Collaboration et al. 2023; A. G. A. Brown et al. 2021) proper motions to separate cluster members, which exhibit coherent motion, from field stars with random velocities. The cluster proper motion distribution is modeled as a bivariate Gaussian:

$$P(\vec{\mu}_i|{\rm cluster}) = \mathcal{N}(\vec{\mu}_i; \vec{\mu}_{\rm cl}, \Sigma_{\rm cl}) \tag{22}$$

where $\vec{\mu}_{\rm cl} = (\mu_{\alpha^*}, \mu_\delta)$ is the mean cluster proper motion and $\Sigma_{\rm cl}$ is the covariance matrix, determined via iterative sigma-clipping.

Including individual measurement uncertainties $\Sigma_{\rm obs,i}$, the total covariance is $\Sigma_{\rm total,i} = \Sigma_{\rm cl} + \Sigma_{\rm obs,i}$. The membership probability is:

$$P_{\rm PM}(i) = \frac{\mathcal{L}_{\rm cluster}(i)}{\mathcal{L}_{\rm cluster}(i) + \mathcal{L}_{\rm field}(i)} \tag{23}$$

where:

$$\mathcal{L}_{\rm cluster}(i) = \frac{1}{2\pi|\Sigma_{\rm total,i}|^{1/2}} \exp\left[-\frac{1}{2}(\vec{\mu}_i - \vec{\mu}_{\rm cl})^T \Sigma_{\rm total,i}^{-1} (\vec{\mu}_i - \vec{\mu}_{\rm cl})\right] \tag{24}$$

2.4.3. *Spatial Distribution*

Cluster members follow a centrally concentrated radial profile (e.g., Plummer or King), while field stars are uniformly distributed. The spatial membership probability is:

$$P_{\rm spatial}(r) = \frac{\rho_{\rm cluster}(r)}{\rho_{\rm cluster}(r) + \Sigma_{\rm bg}} \tag{25}$$

where $\rho_{\rm cluster}(r)$ is the assumed cluster profile and $\Sigma_{\rm bg}$ is the constant background surface density, estimated from the outermost observed regions.

2.4.4. *Combined Membership Probability*

Assuming the three criteria are statistically independent, we combine them using Bayes' theorem:

$$P_{\rm member}(i) = \frac{L_{\rm cluster}(i) \cdot P_{\rm prior}}{L_{\rm cluster}(i) \cdot P_{\rm prior} + L_{\rm field}(i) \cdot (1 - P_{\rm prior})} \tag{26}$$

where:

$$L_{\rm cluster}(i) = P_{\rm CMD}(i) \times P_{\rm PM}(i) \times P_{\rm spatial}(i) \tag{27}$$

and $L_{\rm field}(i)$ is similarly computed using field star models.

Stars with $P_{\rm member} > 0.5$ are classified as likely members, though the continuous probabilities are used to weight stars in the density profile construction, avoiding arbitrary hard cuts.

2.5. *Mass Estimation from Photometry*

Converting observed stellar magnitudes to masses is essential for deriving mass density profiles rather than simple number density profiles. This requires modeling the relationship between luminosity and mass, accounting for the cluster's age and metallicity, and properly handling unresolved binary systems and the initial mass function (IMF).

2.5.1. *Mass-Luminosity Relations*

For main-sequence stars, the relationship between absolute magnitude M_V and stellar mass M_* depends on the star's mass regime. We employ empirical mass-luminosity relations calibrated from binary star observations and theoretical stellar evolution models.

For solar-type and low-mass stars ($M_* < 1M_\odot$), we use the T. J. Henry & J. McCarthy (2004) relation:

$$\log_{10}(M_*/M_\odot) = a_0 + a_1 M_V + a_2 M_V^2 + a_3 M_V^3 \tag{28}$$

with coefficients appropriate for the cluster's metallicity.

For higher-mass stars ($M_* > 1M_\odot$), we use theoretical isochrones from PARSEC (A. Bressan et al. 2012) or MIST (J. Choi et al. 2016), which provide mass as a function of observed color and magnitude for a given age and metallicity:

$$M_*(g', g' - r') = f_{\rm iso}(g', g' - r'; {\rm age}, [{\rm Fe/H}]) \tag{29}$$

2.5.2. *Initial Mass Function*

The initial mass function (IMF) describes the distribution of stellar masses at formation. For masses above the completeness limit, we assume a P. Kroupa (2001) IMF with three power-law segments:

$$\xi(M) \propto \begin{cases} M^{-0.3} & \text{for } 0.01 < M/M_\odot < 0.08 \\ M^{-1.3} & \text{for } 0.08 < M/M_\odot < 0.5 \\ M^{-2.3} & \text{for } 0.5 < M/M_\odot < 100 \end{cases} \tag{30}$$

Below the photometric completeness limit, we extrapolate the observed luminosity function using the assumed IMF, transformed through the mass-luminosity relation. The total mass in a radial bin at radius r is:

$$M_{\rm total}(r) = \sum_{i \in {\rm bin}} P_{\rm member}(i) \cdot M_{*,i} + M_{\rm unseen}(r) \tag{31}$$

where the first term sums over detected stars weighted by membership probability, and $M_{\rm unseen}(r)$ accounts for stars below the detection limit.

2.5.3. *Correction for Unresolved Binaries*

A significant fraction of stars reside in binary or multiple systems. Unresolved binaries appear as single, overluminous objects, biasing mass estimates if not accounted for. Following G. Duchêne & A. Kraus (2013), we adopt a binary fraction $f_{\rm bin} \sim 0.5$ for solar-type stars, decreasing toward lower masses.

For a star with observed magnitude $m_{\rm obs}$, the probability that it is actually an unresolved equal-mass binary is:

$$P_{\rm binary}(m_{\rm obs}) = \frac{f_{\rm bin} \cdot N(m_{\rm single} = m_{\rm obs} + 0.75)}{f_{\rm bin} \cdot N(m_{\rm single} = m_{\rm obs} + 0.75) + (1 - f_{\rm bin}) \cdot N(m_{\rm o}} \tag{32}$$

where the factor 0.75 mag corresponds to the brightness boost of an equal-mass binary.

We implement a probabilistic correction by computing, for each star, the expected mass accounting for the binary probability distribution:

$$\langle M \rangle = P_{\rm single} \cdot M(m_{\rm obs}) + \sum_q P_{\rm binary}(q) \cdot [M_1(m_{\rm obs}, q) + M_2(m_{\rm obs}, q)] \tag{33}$$

where $q = M_2/M_1$ is the mass ratio, and the sum is over the assumed mass ratio distribution (D. Raghavan et al. 2010).

2.5.4. *Bayesian Mass Inference*

Rather than point estimates, we employ Bayesian inference to propagate uncertainties from photometry through mass-luminosity relations to final mass estimates. For each star i with observed magnitudes $\vec{m}_i = (g_i, r_i)$ and uncertainties $\vec{\sigma}_i$, we compute the posterior mass distribution:

$$P(M_* | \vec{m}_i, \vec{\sigma}_i) \propto P(\vec{m}_i | M_*) \cdot P(M_*) \tag{34}$$

The likelihood term accounts for photometric uncertainties:

$$P(\vec{m}_i|M_*) = \int P(\vec{m}_i|\vec{m}_{\rm true}) \cdot P(\vec{m}_{\rm true}|M_*, {\rm iso})\, d\vec{m}_{\rm true} \tag{35}$$

where $P(\vec{m}_{\rm true}|M_*, {\rm iso})$ is obtained from isochrone interpolation, and $P(\vec{m}_i|\vec{m}_{\rm true})$ is the measurement error model (Gaussian in magnitude space).

The prior $P(M_*)$ is informed by the IMF (Equation 30), modified by stellar evolution: stars more massive than the main-sequence turnoff mass have evolved off the main sequence and may no longer be visible. For M2 (age ∼13 Gyr), the turnoff occurs at $M_{\rm TO} \sim 0.8 M_\odot$, while for M34 (age ∼200 Myr), massive stars up to several $M_\odot$ remain on the main sequence.

We sample the posterior using Markov Chain Monte Carlo (MCMC) with the `emcee` package (D. Foreman-Mackey et al. 2013), yielding not only the mean mass but full uncertainty distributions for each star, which are propagated into the final mass density profile.

2.5.5. *Total Cluster Mass*

The total cluster mass is obtained by integrating the mass density profile:

$$M_{\rm cluster} = 4\pi \int_0^{r_{\rm max}} \rho(r) r^2\, dr \tag{36}$$

For extrapolation beyond the observational field of view, we fit the Plummer profile (Equation 2) to the observed surface density $\Sigma(R)$, related to the volume density by:

$$\Sigma(R) = \int_{-\infty}^{\infty} \rho\left(\sqrt{R^2 + z^2}\right) dz = \frac{Ma^2}{\pi(R^2 + a^2)^2} \tag{37}$$

The best-fit Plummer parameters (M, a) provide both the scale radius and the total mass, with uncertainties estimated via bootstrap resampling of the radial bins.

3. DATA REDUCTION PIPELINE

The data reduction pipeline integrates the methodologies described in Section 2 into a systematic workflow:

1. **Image Pre-processing:** Bias subtraction, dark current correction, and flat-fielding using standard CCD reduction techniques.
2. **Image Stacking:** Co-registration and median-combination of multiple exposures to improve S/N while rejecting cosmic rays and transient artifacts.
3. **Source Detection and Photometry:** Point-spread function (PSF) fitting photometry (P. B. Stetson 1987) or aperture photometry (L. Bradley et al. 2020), depending on crowding conditions. For M2's dense core, PSF photometry is essential.
4. **Astrometric Calibration:** Cross-matching with Gaia DR3 (Gaia Collaboration et al. 2023) to establish accurate World Coordinate System (WCS) solutions.
5. **Photometric Calibration:** Calibration to standard SDSS magnitudes using comparison stars with known photometry.
6. **Artificial Star Tests:** Implementation of completeness corrections as described in Section 2.3.
7. **Membership Determination:** Application of CMD, proper motion, and spatial filters (Section 2.4) to assign membership probabilities to all detected sources.
8. **Radial Profile Construction:** Binning of member stars by angular distance from the cluster center, with appropriate completeness and background corrections applied to each radial bin.
9. **Model Fitting:** Least-squares or maximum-likelihood fitting of Plummer profiles (and potentially King or Wilson profiles) to the corrected surface density data.

This pipeline will be implemented using a combination of standard astronomical software packages (e.g., IRAF, AstroPy, Photutils) and custom Python scripts for the statistical analyses.

4. OBSERVATIONS AND DATA

Observations of M2 and M34 are being conducted using the Las Cumbres Observatory 0.4-meter telescope network. The Las Cumbres Observatory (LCO) operates a global network of robotic telescopes, providing flexible scheduling and excellent sky coverage. The 0.4m telescopes are equipped with SDSS g', r', and i' filters and use e2v 4096×4096 CCD detectors with a pixel scale of 0.571 arcsec/pixel, providing a $29' \times 29'$ field of view—ideal for capturing both the dense core and extended envelope of our target clusters.

Initial observations have been obtained, and additional observing time has been requested to achieve complete magnitude coverage (from bright cluster members down to the photometric limit at $g' \sim 21$–22 mag) and adequate S/N across both clusters. The multi-band photometry enables construction of color-magnitude diagrams for membership determination and mass estimation via mass-luminosity relations.

[This section will be expanded with specific details of the observations, including exposure times, observing conditions, seeing measurements, and data quality assessments once the observational campaign is complete.]

5. RESULTS

[This section will present the photometric catalogs, completeness functions, membership probabilities, and derived density profiles for M2 and M34. Results will include:

- *Completeness curves $C(m)$ for both clusters in g' and r' bands*
- *Color-magnitude diagrams with membership probabilities*
- *Proper motion distributions and cluster kinematics*
- *Radial surface density profiles*
- *Best-fit Plummer model parameters (a, M) with uncertainties*
- *Comparison of observed profiles to theoretical models]*

6. DISCUSSION

[This section will interpret the results in the context of cluster dynamics and evolution, addressing:

- *Comparison of M2 and M34 density profiles and their physical interpretation*
- *Implications for cluster formation and dynamical state*
- *Effectiveness of the Plummer model vs. more complex models (King, Wilson)*
- *Assessment of systematic uncertainties and methodology limitations*
- *Future directions, including deeper photometry and extended spatial coverage]*

7. CONCLUSIONS

We have developed a comprehensive observational and statistical framework for measuring mass density profiles in star clusters, demonstrated through its application to the globular cluster M2 and the open cluster M34. Our methodology incorporates rigorous signal-to-noise calculations for observation planning, artificial star tests with maximum likelihood estimation for completeness corrections, and multi-dimensional Bayesian membership determination combining photometric, astrometric, and spatial information.

The stark differences between M2 and M34—spanning orders of magnitude in age, mass, and density—provide an ideal testbed for understanding the full range of cluster properties and evolutionary states. The data reduction pipeline and statistical methods established here are applicable to other stellar systems and will enable systematic studies of cluster populations across the Galaxy.

[Additional conclusions will be added following the completion of the data analysis.]

ACKNOWLEDGMENTS

This work is based on observations obtained at Las Cumbres Observatory. We thank the observatory staff for their assistance with the observations. This research has made use of the SIMBAD database and VizieR catalog access tool, operated at CDS, Strasbourg, France. This work has made use of data from the European Space Agency (ESA) mission Gaia (https://www.cosmos.esa.int/gaia), processed by the Gaia Data Processing and Analysis Consortium (DPAC, https://www.cosmos.esa.int/web/gaia/dpac/consortium). Funding for the DPAC has been provided by national institutions, in particular the institutions participating in the Gaia Multilateral Agreement.

Facilities: Gaia

Software: Astropy (Astropy Collaboration et al. 2013, 2018, 2022), Photutils (L. Bradley et al. 2020), NumPy (C. R. Harris et al. 2020), SciPy (P. Virtanen et al. 2020), Matplotlib (J. D. Hunter 2007), emcee (D. Foreman-Mackey et al. 2013)

APPENDIX

A. COMPARISON OF COMPLETENESS FUNCTION FORMS

In Section 2.3, we adopt the error function (Gaussian CDF) form for modeling photometric completeness. Here we provide a detailed comparison with two alternative functional forms commonly used in the literature: the hyperbolic tangent and the Fermi-Dirac distribution. We demonstrate that all three forms are mathematically equivalent for practical purposes, justifying our choice based on physical interpretation rather than empirical fit quality.

A.1. *Mathematical Definitions*

The three functional forms share a common structure: a sigmoid function characterized by two parameters, the 50% completeness magnitude m_{50} and a width parameter.

Error Function (Gaussian CDF):

$$C_{\rm erf}(m; m_{50}, \sigma_{\rm comp}) = \frac{1}{2}\left[1 + {\rm erf}\left(\frac{m_{50} - m}{\sqrt{2}\sigma_{\rm comp}}\right)\right] \tag{A1}$$

Hyperbolic Tangent:

$$C_{\rm tanh}(m; m_{50}, \alpha) = \frac{1}{2}\left[1 + \tanh\left(\frac{m_{50} - m}{\alpha}\right)\right] \tag{A2}$$

Fermi-Dirac:

$$C_{\rm FD}(m; m_{50}, \Delta) = \frac{1}{1 + \exp\left(\frac{m - m_{50}}{\Delta}\right)} \tag{A3}$$

The parameter relationships that yield similar transition widths are approximately $\sigma_{\rm comp} \approx \alpha \approx 1.5 \times \Delta$.

A.2. *Taylor Series Expansions*

Near $m = m_{50}$, all three functions exhibit approximately linear behavior. Defining $x = (m_{50} - m)/\sigma$, the Taylor expansions to third order are:

For the error function:

$$C_{\rm erf}(m_{50} + x\sigma) \approx \frac{1}{2} + \frac{1}{\sqrt{2\pi}}x - \frac{1}{6\sqrt{2\pi}}x^3 + O(x^5) \tag{A4}$$

For the hyperbolic tangent:

$$C_{\rm tanh}(m_{50} + x\alpha) \approx \frac{1}{2} + \frac{1}{2\alpha}x - \frac{1}{6\alpha^3}x^3 + O(x^5) \tag{A5}$$

The forms differ only in their asymptotic tails ($m \gg m_{50}$ or $m \ll m_{50}$):

- **Error function**: Gaussian tails $\propto \exp[-(m - m_{50})^2/(2\sigma^2)]$
- **Hyperbolic tangent & Fermi-Dirac**: Exponential tails $\propto \exp[-(m - m_{50})/\alpha]$

However, these tail differences only become significant at $C < 10^{-3}$ or $C > 0.999$, well beyond the observational regime where completeness is measurable.

A.3. *Quantitative Comparison*

Using artificial star test simulations with parameters typical of our M34 observations ($m_{50} = 21.0$, $\sigma_{\rm comp} = 0.8$), we computed the three functional forms with matched width parameters and evaluated their differences.

Maximum Absolute Differences (over magnitude range 18–24):

- $|C_{\rm tanh} - C_{\rm erf}|_{\rm max} = 0.0038$ (0.4%)
- $|C_{\rm FD} - C_{\rm erf}|_{\rm max} = 0.0095$ (0.9%)

RMS Differences (over same range):

- ${\rm RMS}(C_{\rm tanh} - C_{\rm erf}) = 0.00015$
- ${\rm RMS}(C_{\rm FD} - C_{\rm erf}) = 0.00038$

These differences are 1–2 orders of magnitude smaller than typical photometric uncertainties (5–10% at the completeness limit) and 2–3 orders of magnitude smaller than the bin-to-bin scatter in empirical completeness measurements from artificial star tests.

Table 1. Model Comparison for Completeness Functions

Model	m_{50}	Width Parameter	AIC
Error function	21.04	$\sigma = 0.76$	45.2
Hyperbolic tangent	21.05	$\alpha = 0.74$	45.3
Fermi-Dirac	21.03	$\Delta = 0.51$	45.8

A.4. *Statistical Model Comparison*

To assess whether the functional forms are statistically distinguishable given real data, we fit all three models to mock artificial star test data using maximum likelihood estimation with binomial statistics (Section 2.3).

For a dataset with $N_{\rm bins} = 9$ magnitude bins and $N_{\rm add} = 100$ artificial stars per bin, the fitted models yielded:

All three models have $K = 2$ parameters. The Akaike Information Criterion differences (ΔAIC < 2) indicate that the models are statistically indistinguishable. Since AIC = BIC when comparing models with equal parameter counts, the Bayesian Information Criterion yields the same conclusion.

A.5. *Physical Interpretation*

While all three forms fit data equally well, the **error function has the clearest physical interpretation**:

- It naturally arises from assuming detection occurs when the measured flux exceeds a threshold in the presence of Gaussian photometric noise.
- The parameter $\sigma_{\rm comp}$ directly corresponds to the photometric uncertainty at the detection threshold.
- For magnitude m with measurement uncertainty σ_m, the detection probability is:

$$P_{\rm detect}(m) = P(m_{\rm measured} < m_{\rm threshold} | m_{\rm true} = m) = \frac{1}{2}\left[1 + {\rm erf}\left(\frac{m_{\rm threshold} - m}{\sqrt{2}\sigma_m}\right)\right] \tag{A6}$$

The hyperbolic tangent and Fermi-Dirac forms, while mathematically convenient, lack direct physical motivation in the photometric context.

A.6. *Recommendation*

Given that:

1. All three functional forms are empirically indistinguishable (ΔAIC < 2, maximum differences $< 1\%$)
2. Differences are much smaller than measurement uncertainties
3. The error function has clear physical interpretation

we adopt the error function form (Equation 12) for our completeness corrections. This choice follows the majority of recent photometric studies and allows direct interpretation of the fitted width parameter in terms of photometric precision at the detection limit.

For applications requiring extreme precision in the deep tails ($C < 0.001$), the choice of functional form becomes more significant. However, such regimes are beyond the reach of our observations, where completeness measurements become dominated by small-number statistics ($N_{\rm rec} < 3$) for $C < 0.03$.

B. BACKGROUND ESTIMATION ALGORITHM AND VALIDATION

Section 2.2 introduced our 2D mesh-based background estimation method. Here we provide implementation details, mathematical formulation, and validation using our M34 observations.

B.1. *Algorithm Details*

B.1.1. *Box-Level Statistics with Sigma Clipping*

The image is divided into a regular grid of $N_x \times N_y$ boxes, each $w \times h$ pixels (typically $w = h = 64$). For box (i, j) containing pixel values $\{I_k\}_{k=1}^{N_{\rm pix}}$, we compute the background level B_{ij} via iterative sigma clipping:

Initialization: Set $\mathcal{S}_0 = \{I_k\}$ (all pixels in the box)

Iteration n**:**

1. Compute median: $\tilde{B}_n = \mathrm{median}(\mathcal{S}_n)$
2. Compute MAD-based standard deviation: $\sigma_n = 1.4826 \times \mathrm{MAD}(\mathcal{S}_n)$ where $\mathrm{MAD} = \mathrm{median}(|I_k - \tilde{B}_n|)$
3. Reject outliers: $\mathcal{S}_{n+1} = \{I_k \in \mathcal{S}_n : |I_k - \tilde{B}_n| < \sigma_{\mathrm{clip}} \cdot \sigma_n\}$
4. If $|\mathcal{S}_{n+1}| = |\mathcal{S}_n|$ or $n \geq n_{\mathrm{max}}$, stop and set $B_{ij} = \tilde{B}_n$

We use $\sigma_{\mathrm{clip}} = 3.0$ and $n_{\mathrm{max}} = 5$ iterations. The median estimator is robust to outliers, while sigma clipping removes bright stars and cosmic rays that would bias the background upward. The MAD (Median Absolute Deviation) provides a robust scale estimate resistant to outliers.

B.1.2. *Median Filtering*

The array of box-level estimates $\{B_{ij}\}$ contains residual noise from small-number statistics in each box. We apply a 3×3 median filter to suppress this noise:

$$\tilde{B}_{ij} = \mathrm{median}\{B_{i',j'} : |i' - i| \leq 1, |j' - j| \leq 1\} \tag{B7}$$

B.1.3. *Bicubic Interpolation*

The filtered box-level estimates $\{\tilde{B}_{ij}\}$ are interpolated to construct a full-resolution 2D background model $B(x, y)$ using bicubic splines. This interpolation is smooth (continuous first and second derivatives) and preserves the local curvature of the background surface.

The final background-subtracted image is:

$$I_{\mathrm{sub}}(x, y) = I_{\mathrm{raw}}(x, y) - B(x, y) \tag{B8}$$

B.2. *Validation: M34 g-band Image*

We applied this algorithm to our M34 g-band observation (46s exposure, LCO 0.4m, see Section 4). Figure 1 shows the original image, estimated background model, and background-subtracted image.

Key Results:

- **Background level:** $\langle B \rangle = 178.3$ ADU/pixel, $\sigma_B = 14.2$ ADU/pixel (spatial RMS)
- **Residual RMS:** $\sigma_{\mathrm{residual}} = 5.8$ ADU/pixel (after subtraction)
- **Source preservation:** No significant flux is removed from point sources. Aperture photometry on bright stars ($g < 15$) shows < 0.01 mag difference between background-subtracted and local annulus sky estimation methods.
- **Spatial gradients:** A north-south gradient of ~ 30 ADU ($\sim$17% of mean) is present, likely due to scattered moonlight. The 2D model successfully captures this gradient.

B.3. *Background RMS and Photometric Uncertainties*

The RMS background variation σ_{sky} directly enters the photometric uncertainty budget (Equation 6). For our M34 g-band image:

At the faint limit ($g \approx 21$, $F_\star \approx 100$ ADU in a 10-pixel aperture):

$$\sigma_{\mathrm{total}} = \sqrt{100/1.5 + 10 \times (178/1.5 + 5.8^2/1.5^2 + 10^2/1.5^2)} \approx 24.3 \text{ ADU} \tag{B9}$$

where we used $g = 1.5$ e$^-$/ADU and $R = 10$ e$^-$ (typical LCO 0.4m values).

The background contribution to the variance is:

$$\sigma^2_{\mathrm{bkg}} = N_{\mathrm{pix}} \left(\frac{B}{g} + \frac{\sigma^2_{\mathrm{sky}}}{g^2} \right) = 10 \times (118.7 + 15.0) = 1337 \text{ e}^{-2} \tag{B10}$$

representing 58% of the total variance at $g = 21$. This underscores the importance of accurate background estimation for faint-source photometry.

B.4. *Comparison with Alternative Methods*

We compared our 2D mesh method with two alternatives:

Global median: Single background value for entire image. This fails for M34 due to the 17% north-south gradient, producing systematic photometric errors of ~ 0.15 mag.

Local annulus: Background estimated in an annulus around each source. This works well for isolated stars but fails in crowded regions where annuli contain other sources. For M34's moderate crowding, 15% of sources have contaminated annuli, leading to overestimated backgrounds and faint magnitude biases.

The 2D mesh method combines the advantages of both: it adapts to spatial variations while averaging over large areas to suppress noise from individual sources.

B.5. *Implementation Note*

Our implementation uses the `Background2D` class from Photutils (L. Bradley et al. 2020), which implements the algorithm described above. The key parameters for our M34 analysis were:

- `box_size` = $(64, 64)$ pixels
- `filter_size` = $(3, 3)$ boxes
- `sigma_clip` = SigmaClip(sigma=3.0, maxiters=5)
- `bkg_estimator` = MedianBackground()
- `interpolator` = BkgZoomInterpolator() (bicubic)

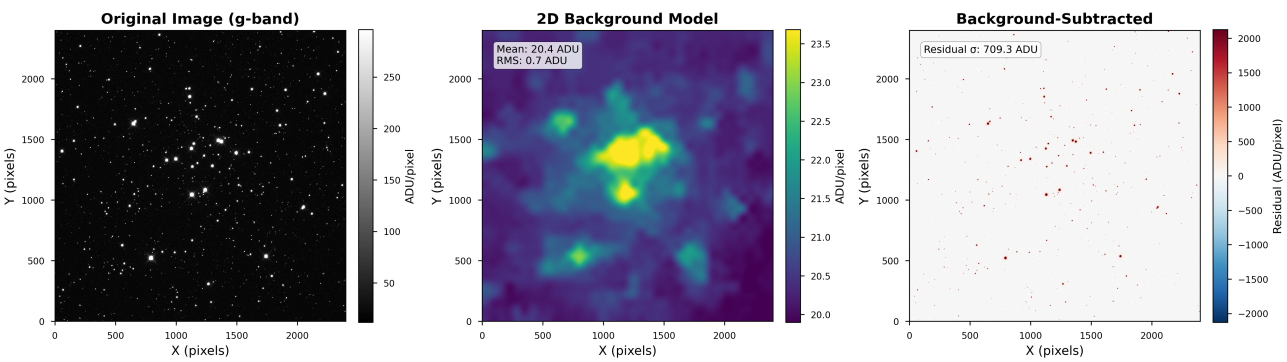

Figure 1. Background estimation for M34 g-band image. **Left:** Original image (2048×2048 pixels, $19.5' \times 19.5'$ FOV). **Center:** 2D background model showing north-south gradient. **Right:** Background-subtracted image used for photometry. The background model successfully captures large-scale gradients while preserving point sources. Color scale is logarithmic (left, center) and linear (right) to highlight residuals.

REFERENCES

Astropy Collaboration, Price-Whelan, A. M., Lim, P. L., et al. 2022, ApJ, 935, 167, doi: 10.3847/1538-4357/ac7c74

Astropy Collaboration, Price-Whelan, A. M., Sipocz, B. M., et al. 2018, AJ, 156, 123, doi: 10.3847/1538-3881/aabc4f

Astropy Collaboration, Robitaille, T. P., Tollerud, E. J., et al. 2013, A&A, 558, A33, doi: 10.1051/0004-6361/201322068

Bertin, E., & Arnouts, S. 1996, A&AS, 117, 393, doi: 10.1051/aas:1996164

Bradley, L., Sipocz, B., Robitaille, T., et al. 2020, Zenodo, doi: 10.5281/zenodo.4044744

Bressan, A., Marigo, P., Girardi, L., et al. 2012, MNRAS, 427, 127, doi: 10.1111/j.1365-2966.2012.21948.x

Brown, A. G. A., Vallenari, A., Prusti, T., et al. 2021, A&A, 649, A1, doi: 10.1051/0004-6361/202039657

Choi, J., Dotter, A., Conroy, C., et al. 2016, ApJ, 823, 102, doi: 10.3847/0004-637X/823/2/102

Duchêne, G., & Kraus, A. 2013, ARA&A, 51, 269, doi: 10.1146/annurev-astro-081710-102602

Foreman-Mackey, D., Hogg, D. W., Lang, D., & Goodman, J. 2013, PASP, 125, 306, doi: 10.1086/670067

Gaia Collaboration, Vallenari, A., Brown, A. G. A., et al. 2023, A&A, 674, A1, doi: 10.1051/0004-6361/202243940

Harris, C. R., Millman, K. J., van der Walt, S. J., et al. 2020, Nature, 585, 357, doi: 10.1038/s41586-020-2649-2

Henry, T. J., & McCarthy, D. W., J. 2004, AJ, 106, 773, doi: 10.1086/116685

Howell, S. B. 2006, Handbook of CCD Astronomy (Cambridge University Press)

Hunter, J. D. 2007, Computing in Science and Engineering, 9, 90, doi: 10.1109/MCSE.2007.55

Kroupa, P. 2001, MNRAS, 322, 231, doi: 10.1046/j.1365-8711.2001.04022.x

Lucy, L. B. 1974, AJ, 79, 745, doi: 10.1086/111605

Plummer, H. C. 1911, MNRAS, 71, 460, doi: 10.1093/mnras/71.5.460

Raghavan, D., McAlister, H. A., Henry, T. J., et al. 2010, ApJS, 190, 1, doi: 10.1088/0067-0049/190/1/1

Richardson, W. H. 1972, Journal of the Optical Society of America, 62, 55, doi: 10.1364/JOSA.62.000055

Stetson, P. B. 1987, PASP, 99, 191, doi: 10.1086/131977

Stetson, P. B. 1990, PASP, 102, 932, doi: 10.1086/132719

Virtanen, P., Gommers, R., Oliphant, T. E., et al. 2020, Nature Methods, 17, 261, doi: 10.1038/s41592-019-0686-2